

A Versatile Theranostic Nanoemulsion for Architecture-Dependent Multimodal Imaging and Dually Augmented Photodynamic Therapy

Yifan Zhang, Shaowei Bo, Tao Feng, Xialing Qin, Yilin Wan, Shanshan Jiang, Chunxiao Li, Jing Lin, Tianfu Wang, Xin Zhou, Zhong-Xing Jiang,* and Peng Huang*

To design a clinically translatable nanomedicine for photodynamic theranostics, the ingredients should be carefully considered. A high content of nanocarriers may cause extra toxicity in metabolism, and multiple theranostic agents would complicate the preparation process. These issues would be of less concern if the nanocarrier itself has most of the theranostic functions. In this work, a poly(ethylene glycol)-boron dipyrromethene amphiphile (PEG-F₅₄-BODIPY) with 54 fluorine-19 (¹⁹F) is synthesized and employed to emulsify perfluorohexane (PFH) into a theranostic nanoemulsion (PFH@PEG-F₅₄-BODIPY). The as-prepared PFH@PEG-F₅₄-BODIPY can perform architecture-dependent fluorescence/photoacoustic/¹⁹F magnetic resonance multimodal imaging, providing more information about the in vivo structure evolution of nanomedicine. Importantly, this nanoemulsion significantly enhances the therapeutic effect of BODIPY through both the high oxygen dissolving capability and less self-quenching of BODIPY molecules. More interestingly, PFH@PEG-F₅₄-BODIPY shows high level of tumor accumulation and long tumor retention time, allowing a repeated light irradiation after a single-dose intravenous injection. The “all-in-one” photodynamic theranostic nanoemulsion has simple composition, remarkable theranostic efficacy, and novel treatment pattern, and thus presents an intriguing avenue to developing clinically translatable theranostic agents.

chemotherapy, and radiotherapy), such as noninvasiveness, low toxicity, repeatability, and avoidance of multidrug resistance. Many photodynamic theranostic nano-platforms that encapsulate both diagnostic agents and photosensitizers (PSs) into a nanocarrier have achieved simultaneous cancer diagnosis and treatment.^[6–9] However, the nanocarrier is just an excipient for drug/gene delivery and the addition of diagnostic agents typically reduces the drug-to-carrier ratio, resulting in a poor loading capability. Moreover, the incorporation of multiple theranostic agents into nanocarrier remarkably complicates the preparation process and increases the metabolic load. Therefore, an ideal theranostic nano-platform is in desperate need whereby the carrier per se exerts most of the therapeutic and diagnostic functions.

Although several imaging modalities are available for cancer diagnosis in the clinic, each of them has inherent limitations. Magnetic resonance (MR) imaging (MRI) offers high spatial resolution and the best soft tissue contrast without tissue depth limits, but it suffers from poor sensitivity and a long imaging time.^[10,11] ¹H MRI is widely used, but the strong background signals from ¹H in the tissues result in low contrast ratio. Fluorescence (FL) imaging (FLI) provides real-time images with high intensity, but its application in large animals and to the clinic settings is limited due to poor light penetration into deep tissues.^[12,13] Photoacoustic (PA) imaging


Theranostics offers a promising approach for the battle against cancer.^[1–3] Among various theranostic systems, photodynamic theranostics integrates photodynamic therapy (PDT) with real-time diagnosis into a nano-platform, thus providing an attractive option for personalized medicine.^[4,5] PDT has advantages over conventional tumor treatment modalities (including surgery,

and radiotherapy), such as noninvasiveness, low toxicity, repeatability, and avoidance of multidrug resistance. Many photodynamic theranostic nano-platforms that encapsulate both diagnostic agents and photosensitizers (PSs) into a nanocarrier have achieved simultaneous cancer diagnosis and treatment.^[6–9] However, the nanocarrier is just an excipient for drug/gene delivery and the addition of diagnostic agents typically reduces the drug-to-carrier ratio, resulting in a poor loading capability. Moreover, the incorporation of multiple theranostic agents into nanocarrier remarkably complicates the preparation process and increases the metabolic load. Therefore, an ideal theranostic nano-platform is in desperate need whereby the carrier per se exerts most of the therapeutic and diagnostic functions.

Dr. Y. Zhang, T. Feng, X. Qin, Y. Wan, S. Jiang, C. Li, Prof. J. Lin, Prof. T. Wang, Prof. P. Huang
Guangdong Key Laboratory for Biomedical Measurements and Ultrasound Imaging
Laboratory of Evolutionary Theranostics
School of Biomedical Engineering
Health Science Center
Shenzhen University
Shenzhen 518060, China
E-mail: peng.huang@szu.edu.cn

Dr. S. Bo, Prof. Z.-X. Jiang
Hubei Province Engineering and Technology Research Center for Fluorinated Pharmaceuticals
School of Pharmaceutical Sciences
Wuhan University
Wuhan 430071, China
E-mail: zxjiang@whu.edu.cn

Prof. X. Zhou
State Key Laboratory for Magnetic Resonance and Atomic and Molecular Physics
Wuhan Institute of Physics and Mathematics
Chinese Academy of Sciences
Wuhan 430071, China

 The ORCID identification number(s) for the author(s) of this article can be found under <https://doi.org/10.1002/adma.201806444>.

DOI: 10.1002/adma.201806444

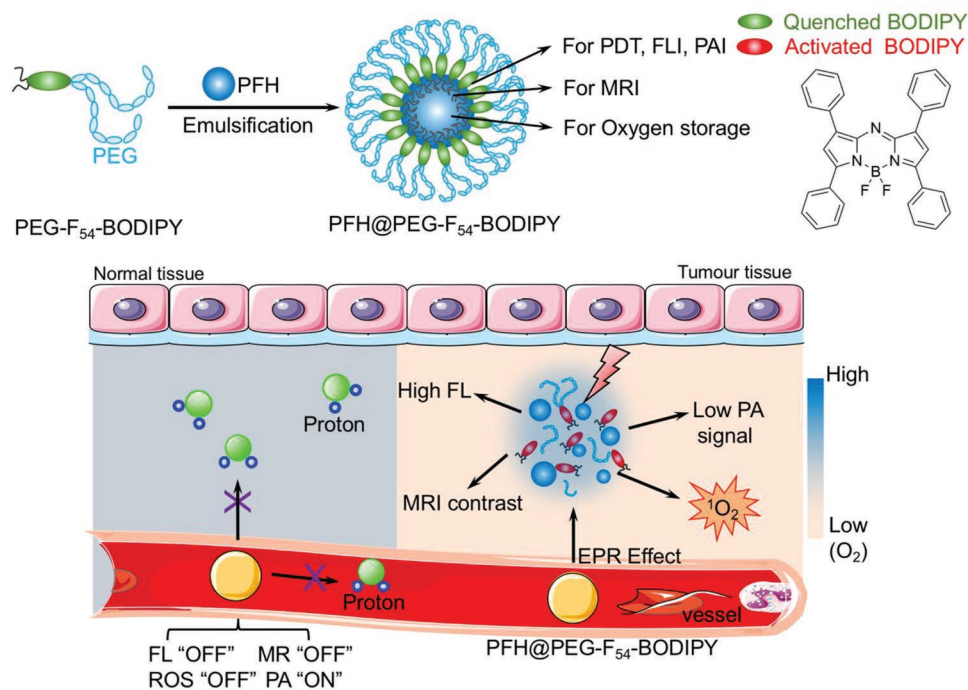
(PAI) possesses high optical imaging contrast and deep tissue penetration;^[14,15] however, an appropriate PAI agent is yet to be developed. Multimodality imaging is thus gaining increasing recognition in cancer diagnostics, as it integrates different information from various sources to provide a more accurate diagnosis than one single technique alone.^[16–20] Combining MRI, FLI, and PAI has the potential to overcome the weakness of each individual technique while simultaneously offering high spatial resolution, contrast, and sensitivity. Nevertheless, current clinical probes for MRI and FLI (e.g., gadolinium-based contrast agents, indocyanine green) usually lack tumor specificity, and so image contrast is affected by extensive background signals. Multimodal imaging signals that can be activated only at the tumor site, provide a feasible approach to solve this problem.^[5]

PDT kills cancer cells by converting tumor oxygen into reactive singlet oxygen ($^1\text{O}_2$) using a PS.^[21,22] However, the hypoxic tumor microenvironment and continuous oxygen consumption during the PDT process can result in an inadequate oxygen supply, which in turn hampers photodynamic efficacy.^[23] Two main strategies have been reported to solve this problem: 1) increasing the oxygen concentration around the PSs via higher oxygen supply;^[24,25] 2) enlarging the distance of PSs in a nano-system to prevent PSs from self-quenching by π - π stacking.^[26]

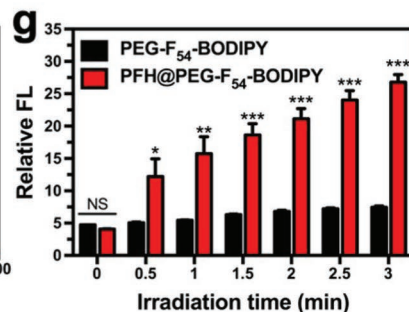
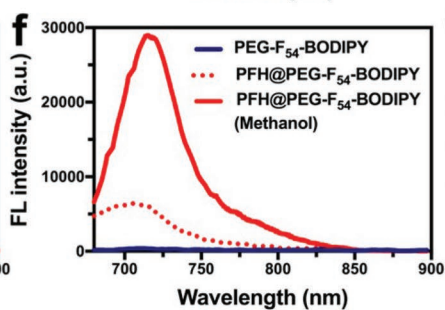
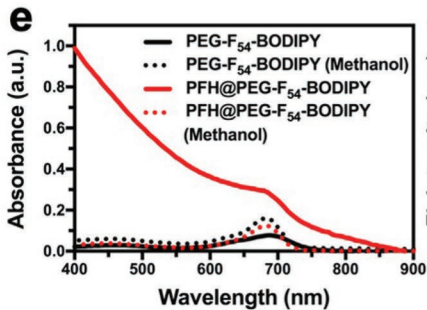
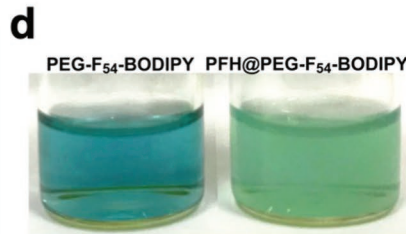
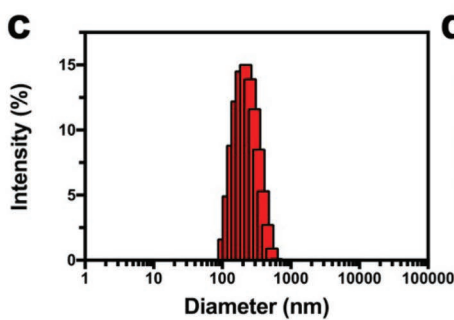
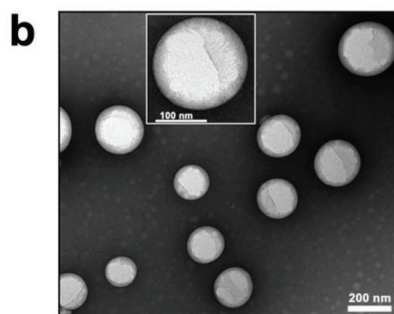
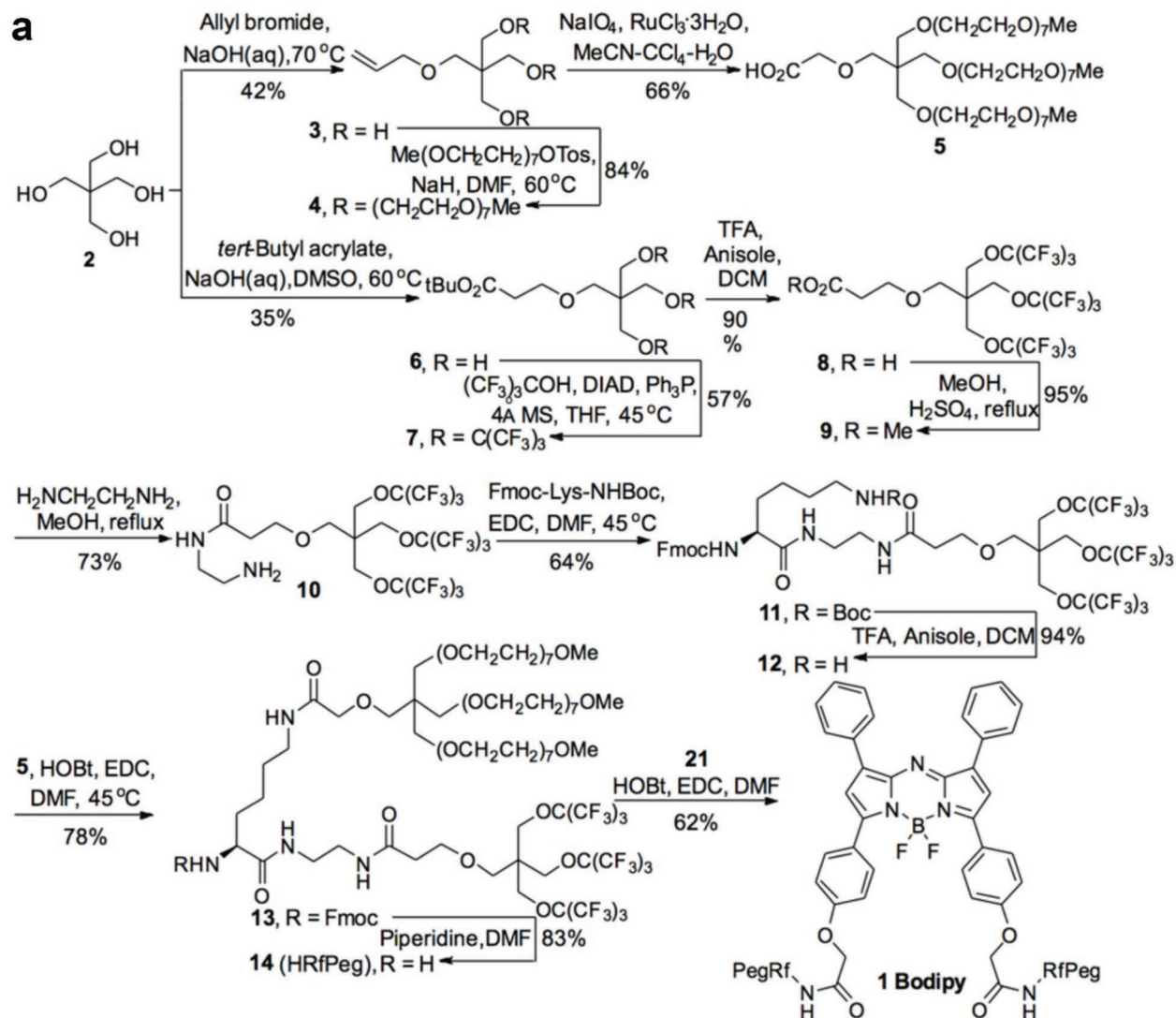
To simultaneously address the above issues, we integrate multimodal imaging signals and PDT function into a poly(ethylene glycol)-boron dipyrromethene amphiphile (PEG- F_{54} -BODIPY) with 54 fluorine-19 (^{19}F), as an “all-in-one” nanocarrier. To enhance the PDT efficacy of BODIPY, perfluorohexane (PFH) is emulsified by the amphiphile to form an oxygen self-supplied nanoemulsion (denoted as PFH@PEG- F_{54} -BODIPY) for FL/PA/MR multimodal imaging guided photodynamic

therapy (Scheme 1). Compared to traditional polymeric drug carriers, the PEG- F_{54} -BODIPY can provide versatile theranostic functions. First, BODIPY is one of the most popular fluorescent chromophores due to its high FL quantum yield and narrow absorption bands.^[27–30] Second, through BODIPY core modifications, the absorption peak of BODIPY redshifts from ≈ 550 nm to the near-infrared (NIR) range (≈ 685 nm), allowing for efficient PAI. Third, the symmetrical ^{19}F with a single ^{19}F -MR signal in the amphiphile can be used for sensitive ^{19}F MRI, which creates much less background noise than ^1H MRI.^[31] Finally, BODIPY has emerged as a new class of PSs for PDT over the past decade.^[32–35] Notably, due to the reduced quenching of BODIPY in PFH@PEG- F_{54} -BODIPY at tumor sites, the FL/ ^{19}F -MR signals of PFH@PEG- F_{54} -BODIPY gradually recovered, while its PA signals underwent an opposite transition. By analyzing the multimodal imaging signals, more information on the drug distribution and assembly level of PFH@PEG- F_{54} -BODIPY could be obtained. Most intriguingly, the PFH@PEG- F_{54} -BODIPY exhibited high tumor tissue accumulation and long tumor retention time (>10 days), which allows us to derive a new treatment paradigm named “Repeated PDT” consisting of one injection and multiple laser irradiations. This PDT protocol could markedly alleviate the treatment burden to patients and the results showed that it could achieve better therapeutic effects than a single laser treatment. Therefore, the as-prepared nanoemulsion (PFH@PEG- F_{54} -BODIPY) can perform FL/PA/MR multimodal imaging and dually augmented PDT for cancer theranostics.

To prepare the versatile nanoemulsion, a convergent synthesis of the BODIPY-based amphiphile (denoted as BODIPY) was first carried out (Figure 1a). Their chemical structures were fully characterized using ^1H nuclear magnetic resonance



Scheme 1. Schematic illustration of versatile theranostic nanoemulsion PFH@PEG- F_{54} -BODIPY, which is self-assembled by a BODIPY amphiphile and perfluorohexane (PFH) (upper panel), as an “all-in-one” nanoplatform for FL/PA/MR multimodal imaging and dual-enhanced PDT (lower panel).



spectroscopy (^1H NMR), ^{13}C NMR, ^{19}F -NMR, and matrix-assisted laser desorption ionization-time of flight mass spectrometry (MALDI-TOF MS) (Figures S1–S4, Supporting Information). Subsequently, BODIPY was utilized as a stabilizer and emulsified PFH (0.5% v/v) into a nanoemulsion by ultrasonication. The final concentration of PFH was 0.26% v/v, so the encapsulation efficiency of PFH was $\approx 52\%$ (Figure S5, Supporting Information). Transmission electron microscopy (TEM) image showed that PFH@PEG- F_{54} -BODIPY has a well-defined spherical structure and average diameter of 180 nm (Figure 1b and inset). The hydrodynamic diameter of PFH@PEG- F_{54} -BODIPY obtained by dynamic light scattering (DLS) measurement was 211.3 nm, and its polydispersity was 0.116 (Figure 1c). The larger size obtained by DLS can be attributed to the fact that DLS measures Brownian motion of particles in solution and includes a few solvent layers.^[36] While PEG- F_{54} -BODIPY aqueous solution was transparent, PFH@PEG- F_{54} -BODIPY solution became translucent due to the formation of nanoemulsion (Figure 1d). These results demonstrated that the PEG- F_{54} -BODIPY can emulsify PFH into spherical and uniform nanoemulsion particles.

We next investigated the photophysical and photochemical properties of PFH@PEG- F_{54} -BODIPY. The UV–vis–NIR absorption spectrum showed that PEG- F_{54} -BODIPY had a sharp absorbance peak at 690 nm, indicating the potential application for PAI (Figure 1e). The absorbance peak of BODIPY blueshifted to 685 nm, possibly due to the reduced BODIPY molecule π – π stacking after emulsification into PFH@PEG- F_{54} -BODIPY.^[37] A similar blueshift was observed when the PEG- F_{54} -BODIPY was dissolved in methanol, because BODIPY dispersed better in methanol than in water, and underwent less π – π stacking (Figure S6a, Supporting Information). Similarly, BODIPY molecule π – π stacking in water induced highly self-quenching of FL (Figure S6b, Supporting Information). However, the FL emission of PFH@PEG- F_{54} -BODIPY was much stronger than that of PEG- F_{54} -BODIPY because of reduced BODIPY molecule π – π stacking after emulsification (Figure 1f). After dissolving in methanol, the FL emission of PFH@PEG- F_{54} -BODIPY nearly sextupled, indicating a partial self-quenching in water. To determine whether the gain of FL was a result of the existence of PFH, we fabricated a series of nanoemulsions with different PFH concentrations. Notably, the all-wavelength absorbance of PFH@PEG- F_{54} -BODIPY increased with PFH concentration, as well as the FL emission under excitation at 660 nm (Figure S7, Supporting Information).

Previous studies on FRET deactivation of $^1\text{O}_2$ generation demonstrated that there was a 0.98 correlation between the Quench of FL and $^1\text{O}_2$ quantum yields.^[38] We thus evaluated the $^1\text{O}_2$ generation of nanoemulsion and PEG- F_{54} -BODIPY as indicated by the FL of Singlet Oxygen Sensor Green, a specific probe for $^1\text{O}_2$ (Figure 1g). Here, PFH@PEG- F_{54} -BODIPY

achieved much higher $^1\text{O}_2$ generation than PEG- F_{54} -BODIPY, and the $^1\text{O}_2$ quantum yield was calculated as 0.57 referring to a reported method (Table S1, Supporting Information).^[39] Reduced BODIPY molecular π – π stacking also influenced ^{19}F -MR signals: there were 54 fluorines in each amphiphile, which exhibited a sharp singlet ^{19}F -MR peak in methanol (Figure S8, Supporting Information). However, the ^{19}F -MR signal detected from its aqueous solution was much weaker, indicating a shorter T_2 relaxation time as a consequence of BODIPY molecule π – π stacking in water.^[40] These experiments demonstrated that emulsification of PFH into nanoemulsions effectively reduces BODIPY self-quenching in water and thus enhance the FL, ^{19}F -NMR signals and $^1\text{O}_2$ quantum yield. The further FL signal recovery of nanoemulsion in methanol indicates an “off-to-on” FL transition after the complete disassociation of the nanoemulsion in vivo.

To further investigate the influence of emulsification into PFH@PEG- F_{54} -BODIPY on BODIPY imaging properties, we performed in vitro FL/PA/MR multimodal imaging. The echo signals of PFH@PEG- F_{54} -BODIPY were threefold higher than that of PEG- F_{54} -BODIPY due to the ultrasonic (US) imaging contrast properties of PFH (Figure 2a,b).^[41] Similar to the results obtained using a FL spectrophotometer, the FL signal of PEG- F_{54} -BODIPY under 660 nm excitation was completely quenched due to the π – π stacking of BODIPY molecules. After emulsification into PFH@PEG- F_{54} -BODIPY, the signals partially recovered and further enhanced in methanol (Figure 2c). As BODIPY in the nanoemulsion was still partially self-quenched, a proportion of the energy normally transformed to FL and $^1\text{O}_2$ generation was released elsewhere. Under the laser irradiation, the energy was dissipated thermally, but the temperature was lower than 42 °C, which is not sufficient to induce cell death (Figure S9, Supporting Information). As PAI is related to thermal expansion, PFH@PEG- F_{54} -BODIPY generated strong PA signals, linearly and proportional to concentration (Figure 2d,e). PA signals decreased up to 30-fold after methanol was added to disrupt the structure and dissolve BODIPY. Therefore, the architecture-dependent FL quenching of BODIPY is a requisite for PA properties. As shown in Table S2 in the Supporting Information, both BODIPY and PFH in the PFH@PEG- F_{54} -BODIPY exhibited strong ^{19}F -MR signals (T_1 of BODIPY, 375 ms; T_2 of BODIPY, 28 ms; T_1 of PFH, 1040 ms; T_2 of PFH, 181 ms). Moreover, the signal of BODIPY in PFH@PEG- F_{54} -BODIPY was also significantly enhanced compared to that of PEG- F_{54} -BODIPY, which might be attributed to the extended T_2 (T_2 of PEG- F_{54} -BODIPY: 14.9 ms). The ^{19}F -MR signals also partially recovered in the PFH@PEG- F_{54} -BODIPY due to the milder self-quenching than that in the PEG- F_{54} -BODIPY (Figure 2f,g, Figure S10, Supporting Information). These results demonstrated the great potential of PFH@PEG- F_{54} -BODIPY to perform architecture-dependent FL/PA/MR multimodal imaging in vivo.

Figure 1. a) Synthesis route of PEG- F_{54} -BODIPY amphiphile. b) TEM image (inset) and c) size distribution of PFH@PEG- F_{54} -BODIPY (20 μM BODIPY, 0.5% v/v PFH). d) Photograph of PEG- F_{54} -BODIPY and PFH@PEG- F_{54} -BODIPY (20 μM BODIPY, 0.5 v/v% PFH). e) UV–vis–NIR absorption and f) FL emission spectra of PEG- F_{54} -BODIPY and PFH@PEG- F_{54} -BODIPY in water or methanol. g) Singlet oxygen generation of PEG- F_{54} -BODIPY and PFH@PEG- F_{54} -BODIPY following irradiation with a 660 nm laser at a power density of 200 mW cm^{-2} for the indicated time. The values represent the means \pm s.d. ($n = 3$, NS, not significant; * $P < 0.05$, ** $P < 0.01$, *** $P < 0.001$ vs BODIPY).

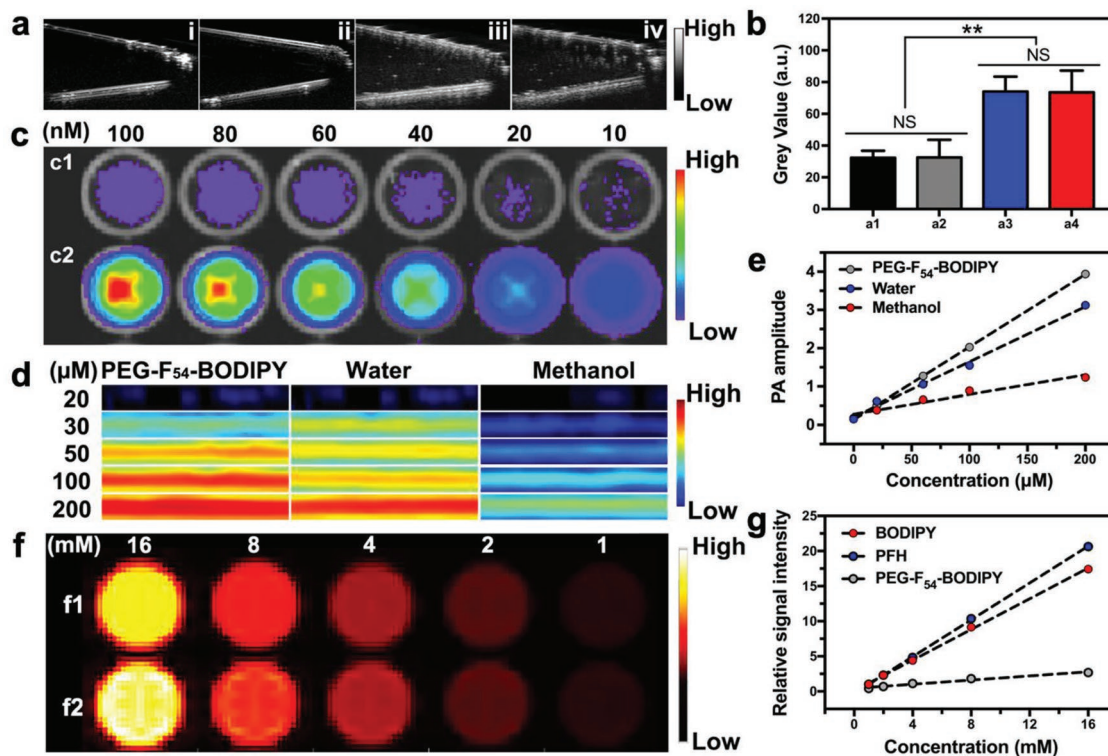


Figure 2. a) In vitro Ultrasonic (US) images and b) the corresponding gray values of water, PEG-F₅₄-BODIPY, PFH@PEG-F₅₄-BODIPY, and oxygenated PFH@PEG-F₅₄-BODIPY, from left to right (20 μM BODIPY, 0.5 v/v% PFH). The values represent the means ± s.d. (*n* = 3; NS, not significant; ***P* < 0.01). c) In vitro FL images of PFH@PEG-F₅₄-BODIPY in different solvents (c1: water, c2 methanol). d) In vitro PA images and e) the corresponding PA amplitudes of PFH@PEG-F₅₄-BODIPY in different solvents (d1: water, d2 methanol). f) In vitro MR images and g) the corresponding MR signal intensity of PFH@PEG-F₅₄-BODIPY (f1: BODIPY, f2: PFH).

We then investigated the FL properties of PFH@PEG-F₅₄-BODIPY in human melanoma A375 cells. After 24 h of incubation, PFH@PEG-F₅₄-BODIPY red FL was visible in the cytoplasm (Figure 3a), indicating efficient cell uptake and FL capability. To quantitatively investigate the FL in cancer cells, cells incubated with PFH@PEG-F₅₄-BODIPY and PEG-F₅₄-BODIPY were analyzed by flow cytometry. Results showed that the BODIPY FL intensity increased as a function of time in both groups (Figure 3b–d). However, the PEG-F₅₄-BODIPY group exhibited much higher FL than the PFH@PEG-F₅₄-BODIPY group. To examine whether this difference was a result of the cell uptake efficiency or FL self-quenching, the cancer cells were collected and lysed by ultrasonication to release PEG-F₅₄-BODIPY. The measurements obtained using a FL microplate showed that before cell lysis, the FL of the PEG-F₅₄-BODIPY group was nearly fivefold higher than the PFH@PEG-F₅₄-BODIPY group (Figure 3e). After ultrasonication, the FL of the PFH@PEG-F₅₄-BODIPY group recovered and almost equaled to that of PEG-F₅₄-BODIPY group. These results indicated that the PFH@PEG-F₅₄-BODIPY uptake efficiency was similar to that of PEG-F₅₄-BODIPY, but that the FL of PFH@PEG-F₅₄-BODIPY was largely quenched inside the cells. This deduction was contradictory to our previous results (Figures 1e and 3c), in which the self-quenching of BODIPY was partially relieved in PFH@PEG-F₅₄-BODIPY. Considering that there were abundant proteins (e.g., albumin, low density lipoprotein) in the cell culture media, we investigated the FL changes of BODIPY

after incubation with cell media and found that after 5 min of incubation, the FL of PEG-F₅₄-BODIPY markedly recovered while that of PFH@PEG-F₅₄-BODIPY remained almost the same (Figure 3f). This phenomenon could be because that the π - π stacking interactions that induced FL self-quenching were much weaker after proteins in the medium solubilized BODIPY amphiphiles. The stability of the nanoemulsion in the medium and partial self-quenching of FL in cancer cells suggested that the PFH@PEG-F₅₄-BODIPY FL might slowly increase as the emulsion ruptured in vivo. As PA signals depended on the self-quenching of BODIPY, opposite change of PA signal was rationally expected.

The cytotoxicity and PDT effect of PFH@PEG-F₅₄-BODIPY were investigated next in vitro. First, the generation of reactive oxygen species (ROS) including ¹O₂ from PDT was stained using a commercial probe (carboxy-H₂DCFDA) in A375 cells (Figure S11, Supporting Information). After penetrating into the cytoplasm and encountering ROS, the probe would emit intense green FL. Without light irradiation, cells treated with PBS, PEG-F₅₄-BODIPY, and PFH@PEG-F₅₄-BODIPY showed negligible FL (data not shown). After 5 min laser irradiation at 660 nm laser (power density: 200 mW cm⁻²), >80% of cells treated with PFH@PEG-F₅₄-BODIPY emitted green FL, which was significantly higher than that of the free BODIPY group, indicating a higher oxidative stress mediated by PFH@PEG-F₅₄-BODIPY. Next, calcein-AM/PI double staining was carried out to semiquantitatively assess the PDT enhancement

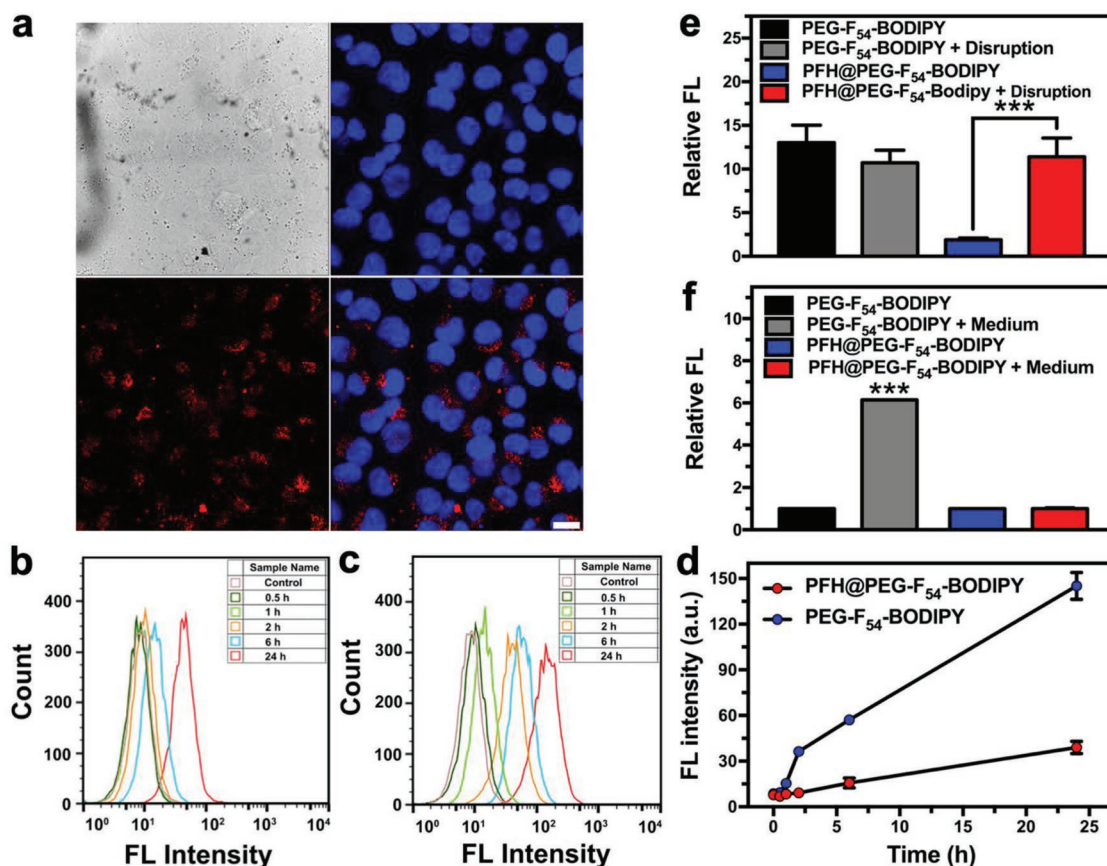


Figure 3. a) Confocal laser scanning microscopy images of A375 tumor cells stained with Hoechst 333342 after 24 h incubation with the PFH@PEG-F₅₄-BODIPY. Scale bar = 10 μm. b,c) Flow-cytometry analysis of PFH@PEG-F₅₄-BODIPY and PEG-F₅₄-BODIPY FL inside A375 cells, respectively. d) Changes in BODIPY FL intensity in cells as a function of incubation time. e) Relative FL of PFH@PEG-F₅₄-BODIPY or PEG-F₅₄-BODIPY after 5 min US irradiation to the corresponding untreated groups (US power: 3 W). f) Relative FL of PFH@PEG-F₅₄-BODIPY or PEG-F₅₄-BODIPY 24 h after incubation with DMEM (10% v/v fetal bovine serum) to the corresponding untreated groups (Ex/Em: 685/715 nm). Values represent the means ± s.d. (*n* = 3 for e, *n* = 5 for f, ****P* < 0.001).

efficacy (Figure 4a,b). The green (calcein-AM) and red (PI) FL represented live and dead (or apoptotic) cells, respectively. Similar to ROS staining, both PFH@PEG-F₅₄-BODIPY and PEG-F₅₄-BODIPY elicited negligible red FL outside the light spot, indicating good compatibility of the BODIPY amphiphile. After light irradiation (5 × 10⁻⁶ M BODIPY; 300 J cm⁻² laser power), >50% tumor cells treated with PFH@PEG-F₅₄-BODIPY were killed and emitted red FL, which was much more than that of PEG-F₅₄-BODIPY group. We then conducted a cell viability counting assay to quantitatively investigate the enhanced PDT efficacy. Without light irradiation, both PFH@PEG-F₅₄-BODIPY and PEG-F₅₄-BODIPY showed negligible cytotoxicity up to 10 × 10⁻⁶ M against A375 melanoma cancer cells (Figure 4c). The PDT efficacy in vitro was found to be BODIPY dose and light dose-dependent (Figure 4d,e). In the absence of oxygen, the oxygenated PFH@PEG-F₅₄-BODIPY remained high PDT efficacy, further indicating the oxygen storage capability of PFH (Figure S12, Supporting Information). PFH@PEG-F₅₄-BODIPY was much more cytotoxic than PEG-F₅₄-BODIPY using the same light irradiation dose, as indicated by intracellular ROS generation and live/dead cell staining images. Less than 40% of tumor cells treated with

PFH@PEG-F₅₄-BODIPY remained alive after 5 min irradiation at the BODIPY dose of 10 × 10⁻⁶ M, while the viability of the PEG-F₅₄-BODIPY group was ≈70%. Because a similar amount of PFH@PEG-F₅₄-BODIPY was incorporated into tumor cells compared to PEG-F₅₄-BODIPY, the significantly higher ROS production and cell mortality of the PFH@PEG-F₅₄-BODIPY group indicated successful enhancement of PDT efficacy due to reduced quenching of BODIPY in nanoemulsions. The O₂ concentration in the cell culture was ≈21% (equivalent to air), and so the oxygenation of PFH would have been a negligible factor contributing to PDT efficacy enhancement. The hypoxic environment of malignant tumors indicated tremendous potential of PDT enhancement via oxygen storage capability of PFH.^[42]

We next examined the unique quality that PFH@PEG-F₅₄-BODIPY was intrinsically suited for in vivo PA/FL/MR multimodal imaging using an A375 melanoma xenograft model. The particle size of PFH@PEG-F₅₄-BODIPY was ≈180 nm (Figure 1a,b), which is in the optimal range for an enhanced permeation and retention (EPR) effect.^[43,44] Moreover, due to its architecture-dependent FL property, PFH@PEG-F₅₄-BODIPY is particularly suitable to function as an activatable FL probe that stays silent (i.e., off state) in the blood

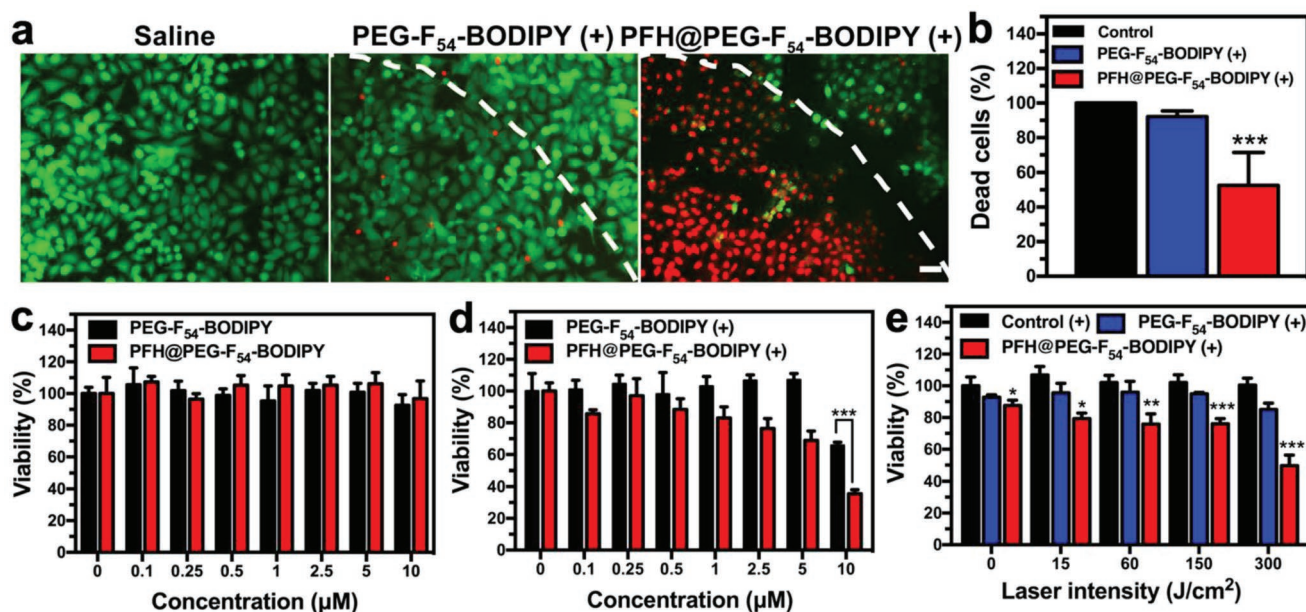


Figure 4. a) FL images of live/dead cell staining on A375 tumor cells after 12 h incubation with fresh medium, PEG-F₅₄-BODIPY or PFH@PEG-F₅₄-BODIPY and exposure to a 660 nm laser at the power density of 200 mW cm⁻² for 10 min (5 × 10⁻⁶ M BODIPY). A clear laser spot can be seen in the irradiated PFH@PEG-F₅₄-BODIPY group. Scale bar = 50 μm. b) Quantitative analysis of the dead cells proportion according to (a). c) Relative viability of A375 tumor cells treated with PFH@PEG-F₅₄-BODIPY or PEG-F₅₄-BODIPY at various doses. d) Relative viability of A375 tumor cells treated with PFH@PEG-F₅₄-BODIPY or PEG-F₅₄-BODIPY at various doses after irradiation with a 660 nm laser at a power density of 200 mW cm⁻² for 5 min. e) Relative viability of A375 tumor cells treated with PFH@PEG-F₅₄-BODIPY or PEG-F₅₄-BODIPY (5 × 10⁻⁶ M of BODIPY) after irradiation with a 660 nm laser at different laser intensities for 5 min. Values represent the means ± s.d. (n = 6 for a–c, n = 3 for e; NS, not significant; *P < 0.05, **P < 0.01, ***P < 0.001 vs BODIPY + Laser).

circulation to minimize background FL. The quenching status of PFH@PEG-F₅₄-BODIPY in blood was further verified by the recovery of FL following the addition of SDS (Sodium dodecyl sulfate) (Figure S13, Supporting Information). Upon accumulation at the tumor site via the size-mediated EPR effect, PFH@PEG-F₅₄-BODIPY was expected to gradually dissociate apart as a consequence of demulsification and solubilization of the BODIPY amphiphile by proteins in the tumor matrix, followed by the recovery of FL signal (i.e., on state). Conversely, the PA signals of PFH@PEG-F₅₄-BODIPY would undergo “on-to-off” transduction due to the relief of self-quenching after accumulation at the tumor site. As expected, we found that PFH@PEG-F₅₄-BODIPY exhibited a significantly lower FL signal in the normal tissues than PEG-F₅₄-BODIPY after intravenous injection (Figure 5a,b, Figure S14, Table S3, Supporting Information). Ex vivo imaging further confirmed the preferential uptake of PFH@PEG-F₅₄-BODIPY in the melanoma tumors compared to healthy cells (Figure 5c,d). The PFH@PEG-F₅₄-BODIPY FL signal at tumor sites increased about 40-fold within 24 h and then gradually decreased, while the PA signal reached a peak at ≈1 h and reduced to an undetectable level at 24 h (Figure 5e,f). Interestingly, the FL signals increased again 7–8 days after injection, and then slowly decreased and were maintained at half of the peak intensity by day 11 (Figure S15, Supporting Information). This long tumor retention time was probably due to the high BODIPY ¹⁹F content, but the detailed mechanism is yet to be illustrated.^[45] Both BODIPY and PFH showed strong ¹⁹F-MR signals at tumor sites close to the skin after intratumoral injection (Figure 5g). The echo signals of

PFH@PEG-F₅₄-BODIPY also augmented due to the gradual evaporation of PFH in vivo (Figure S16, Supporting Information). Overall, we found that PFH@PEG-F₅₄-BODIPY acts as an activatable FL probe that produces minimal background signals in the bloodstream and recovers FL after its dissociation at tumor sites. PFH@PEG-F₅₄-BODIPY possesses architecture-dependent “on/off” photoacoustic transduction. This feature can assist the real-time acquisition of structural information at tumor sites, and simultaneously served as a MR signal intensifier.

PDT is an established treatment modality for superficial malignant tumors, and has applications in dermatology, ophthalmology, and other fields.^[46] However, to treat deep and solid tumors, PDT efficacy suffers from several intrinsic limitations, including tumor hypoxia, PS distribution and self-quenching, and light penetration depth.^[47,48] With the guidance of FL/PA/MR multimodal imaging, PFH@PEG-F₅₄-BODIPY is a promising strategy to significantly enhance the PDT efficiency via the two different pathways as previously described. To investigate the PDT enhancement, we intravenously injected oxygenated PFH@PEG-F₅₄-BODIPY or PEG-F₅₄-BODIPY into an A375 melanoma xenograft model with tumor volume of ≈80 mm³ 24 h before light treatment. To enhance the hypoxic environment of melanoma tumors, nanoemulsions with high PFH content delivered together with ultrasound irradiation for 30 min immediately before light treatment (Figures S17 and S18, Supporting Information).^[25] Strong green FL was observed in the groups receiving both PFH@PEG-F₅₄-BODIPY and light irradiation, suggesting the severe cell apoptosis of tumor

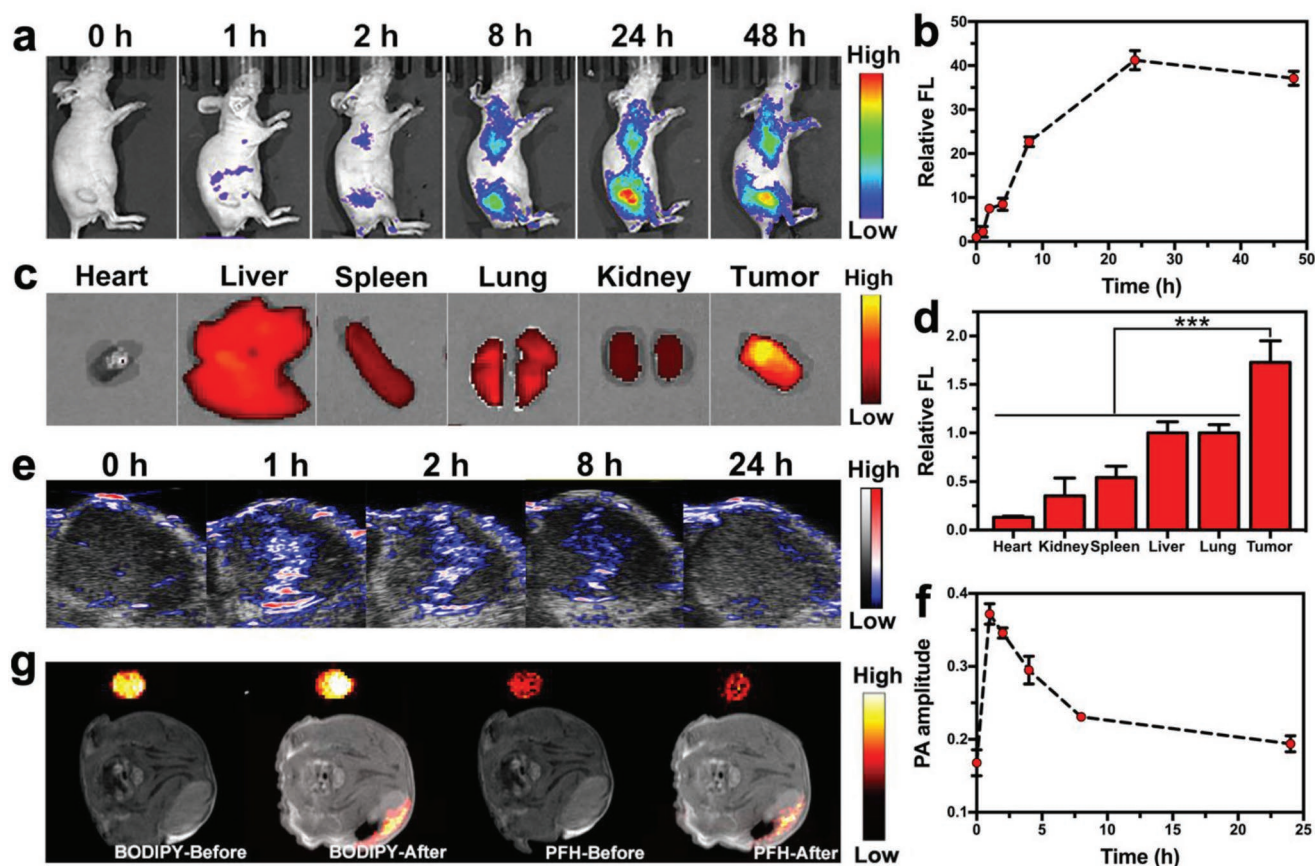


Figure 5. a) In vivo NIR FL images and b) semiquantitative analysis of A375 tumor accumulation of BODIPY after intravenous injection of PFH@PEG-F₅₄-BODIPY. c) Ex vivo FL images and d) semiquantitative analysis of major organs from A375 tumor-bearing mice 24 h after intravenous injection of PFH@PEG-F₅₄-BODIPY. Values represent the means \pm s.d. ($n = 3$, $***P < 0.001$ for tumors compared to other organs). e) Representative photoacoustic imaging and f) semiquantitative analysis of A375 tumor after intravenous injection of PFH@PEG-F₅₄-BODIPY. g) ¹⁹F magnetic resonance imaging of the A375 tumor before and 30 min after intratumoral injection of PFH@PEG-F₅₄-BODIPY.

cells, while only moderate apoptosis was observed in the PEG-F₅₄-BODIPY plus light irradiation group (Figure 6a). Likewise, H&E staining showed a marked hiatus in the cell spaces, nuclei shrinkage, karyorrhexis, and plasmatorrhexis in the PFH@PEG-F₅₄-BODIPY plus light irradiation group, while melanoma cells from other groups retained normal cellular morphology (Figure 6b). These results indicate efficient cell destruction mediated by PFH@PEG-F₅₄-BODIPY.

We finally evaluated the PDT efficacy of PFH@PEG-F₅₄-BODIPY by measuring the tumor volume every two days after treatment in each group (Figure 6c,d). Because of the long tumor retention time of PFH@PEG-F₅₄-BODIPY in tumors, a new treatment paradigm called “repeated PDT” was used to augment the PDT efficiency. Here, one injection of PFH@PEG-F₅₄-BODIPY was followed by light treatment every 5 days. Tumors in saline and PFH@PEG-F₅₄-BODIPY groups grew at a similar rate, whereas the saline plus laser and BODIPY plus laser groups grew at a slightly lower rate probably due to the repeated laser treatment, but there were no statistically significant differences between these four groups according to the ANOVA analysis. Animals within these groups were euthanized in succession within ≈ 30 days due to an extensive tumor burden or tumor-related cachexia. On the contrary, the

PFH@PEG-F₅₄-BODIPY plus light treatment group exhibited much slower tumor growth and 70% of mice survived 40 days (Figure S19, Supporting Information). In the repeated PDT group, all treated mice survived >40 days, and one of the treated tumors was eliminated on day 20 by ulceration (data not shown). Taken together, PFH@PEG-F₅₄-BODIPY markedly enhances the PDT efficacy of BODIPY through the two different approaches: 1) increasing oxygen loading around the PSs via its high oxygen dissolving capacity; 2) enlarging the distance of PSs after being encapsulated into emulsions to prevent PSs from self-quenching by π - π stacking. No significant changes were observed in body weight, normal tissue morphology, or serum chemistry in all these treatment groups (Figures S20–S22, Supporting Information). In addition, no obvious hemolysis was observed for the BODIPY amphiphile ($3\text{--}10 \times 10^{-6}$ M) in the blood (Figure S23, Supporting Information). These results indicated good biocompatibility of this versatile nanotheranostic platform.

To summarize, we have developed a novel amphiphile that possesses several unique and favorable traits rendering it suitable as a cancer theranostic agents: 1) distinct architecture-dependent fluorescent, photoacoustic, and magnetic resonance properties; 2) intrinsic ability for enhanced PDT via two different

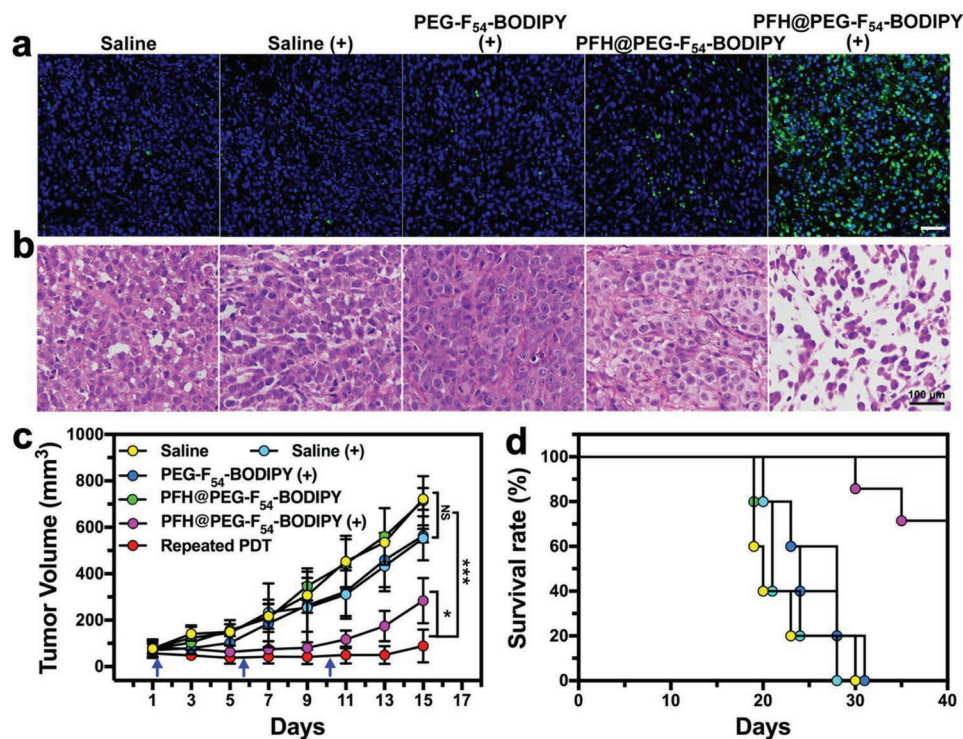


Figure 6. a) TUNEL staining images for DNA damage and b) hematoxylin and eosin (H&E) staining images for cellular morphology in each group to determine the PDT efficiency. DAPI counterstaining indicates the tumor nuclear region. Scale bar = 100 μm . c) Tumor growth curves and d) survival curves of A375 melanoma tumor-bearing mice received the PDT treatment. Scale bar = 100 μm . The blue arrows indicated the laser irradiation in saline plus laser and repeated PDT group. The values represent the means \pm s.d. ($n = 7$ for PFH@PEG-F₅₄-BODIPY plus laser group, $n = 5$ for other groups; * $P < 0.05$, *** $P < 0.001$).

pathways; 3) excellent emulsification ability for forming nanoemulsions; 4) long tumor retention time for repeated PDT treatment; and 5) good biocompatibility. We have demonstrated in a melanoma cancer xenograft model that the as-prepared PFH@PEG-F₅₄-BODIPY nanoemulsion may be used as: 1) an activatable nanoprobe to increase the sensitivity of FL/PA/MR multimodal imaging for tumor detection, and 2) an oxygen carrier and PS quenching reliever to achieve highly efficient PDT on hypoxic solid tumors via a single injection of drug. The superior imaging capability of PFH@PEG-F₅₄-BODIPY can be further utilized to monitor the real-time in vivo behavior and assembly state of the nanoemulsion for optimized treatment. The results reported here have consolidated our design of using the nano-carrier in the theranostic nanoparticles to exert sophisticated and versatile “all-in-one” theranostic functions.

Supporting Information

Supporting Information is available from the Wiley Online Library or from the author.

Acknowledgements

Y.Z., S.B., and T.F. contributed equally to this work. This work was financially supported by the Fok Ying-Tong Education Foundation for Young Teachers in the Higher Education Institutions of China (161032), the Basic Research Program of Shenzhen (JCYJ20170412111100742), the

China Postdoctoral Science Foundation (2018M633138), the National Natural Science Foundation of China (51573096, 31771036, 51703132, and 21572168), the Guangdong Province Natural Science Foundation of Major Basic Research and Cultivation Project (2018B030308003), and the National Key Research and Development Program of China (2016YFC1304704). The authors thank Instrumental Analysis Center of Shenzhen University (Xili Campus). Female athymic BALB/c nude mice were used in accordance with the regulations of the Animal Ethical and Welfare Committee of Shenzhen University (AEWC-SZU).

Conflict of Interest

The authors declare no conflict of interest.

Keywords

BODIPY amphiphiles, multimodal imaging, nanoemulsion, perfluorocarbon, photodynamic theranostics

Received: October 5, 2018

Revised: February 3, 2019

Published online: March 25, 2019

- [1] H. Chen, W. Zhang, G. Zhu, J. Xie, X. Chen, *Nat. Rev. Mater.* **2017**, *2*, 17024.
[2] W. Fan, B. Yung, P. Huang, X. Chen, *Chem. Rev.* **2017**, *117*, 13566.

- [3] S. Wang, J. Lin, Z. Wang, Z. Zhou, R. Bai, N. Lu, Y. Liu, X. Fu, O. Jacobson, W. Fan, J. Qu, S. Chen, T. Wang, P. Huang, X. Chen, *Adv. Mater.* **2017**, *29*, 1701013.
- [4] H. Tong, Y. Chen, Z. Li, H. Li, T. Chen, Q. Jin, J. Ji, *Small* **2016**, *12*, 6223.
- [5] J. F. Lovell, T. W. Liu, J. Chen, G. Zheng, *Chem. Rev.* **2010**, *110*, 2839.
- [6] J. Li, F. Cheng, H. Huang, L. Li, J. J. Zhu, *Chem. Soc. Rev.* **2015**, *44*, 7855.
- [7] F. M. Kievit, M. Zhang, *Adv. Mater.* **2011**, *23*, H217.
- [8] Y. Li, T. Y. Lin, Y. Luo, Q. Liu, W. Xiao, W. Guo, D. Lac, H. Zhang, C. Feng, S. Wachsmann-Hogiu, J. H. Walton, S. R. Cherry, D. J. Rowland, D. Kukis, C. Pan, K. S. Lam, *Nat. Commun.* **2014**, *5*, 4712.
- [9] P. Huang, J. Lin, X. Wang, Z. Wang, C. Zhang, M. He, K. Wang, F. Chen, Z. Li, G. Shen, D. Cui, X. Chen, *Adv. Mater.* **2012**, *24*, 5104.
- [10] L. Li, W. Jiang, K. Luo, H. Song, F. Lan, Y. Wu, Z. Gu, *Theranostics* **2013**, *3*, 595.
- [11] Y. Lu, Y.-J. Xu, G.-b. Zhang, D. Ling, M.-q. Wang, Y. Zhou, Y.-D. Wu, T. Wu, M. J. Hackett, B. Hyo Kim, H. Chang, J. Kim, X.-T. Hu, L. Dong, N. Lee, F. Li, J.-C. He, L. Zhang, H.-Q. Wen, B. Yang, S. Hong Choi, T. Hyeon, D.-H. Zou, *Nat. Biomed. Eng.* **2017**, *1*, 637.
- [12] G. Hong, A. L. Antaris, H. Dai, *Nat. Biomed. Eng.* **2017**, *1*, 0010.
- [13] K. Zhang, Y. J. Gao, P. P. Yang, G. B. Qi, J. P. Zhang, L. Wang, H. Wang, *Adv. Healthcare Mater.* **2018**, *7*, 1800344.
- [14] S. Wang, J. Lin, T. Wang, X. Chen, P. Huang, *Theranostics* **2016**, *6*, 2394.
- [15] Y. Liu, S. Wang, Y. Ma, J. Lin, H. Y. Wang, Y. Gu, X. Chen, P. Huang, *Adv. Mater.* **2017**, *29*, 1606129.
- [16] J. Lin, M. Wang, H. Hu, X. Yang, B. Wen, Z. Wang, O. Jacobson, J. Song, G. Zhang, G. Niu, P. Huang, X. Chen, *Adv. Mater.* **2016**, *28*, 3273.
- [17] W. H. Chen, C. X. Yang, W. X. Qiu, G. F. Luo, H. Z. Jia, Q. Lei, X. Y. Wang, G. Liu, R. X. Zhuo, X. Z. Zhang, *Adv. Healthcare Mater.* **2015**, *4*, 2247.
- [18] Y. Wang, T. Yang, H. Ke, A. Zhu, Y. Wang, J. Wang, J. Shen, G. Liu, C. Chen, Y. Zhao, H. Chen, *Adv. Mater.* **2015**, *27*, 3874.
- [19] C. Li, Y. Zhang, Z. Li, E. Mei, J. Lin, F. Li, C. Chen, X. Qing, L. Hou, L. Xiong, H. Hao, Y. Yang, P. Huang, *Adv. Mater.* **2018**, *30*, 1706150.
- [20] P. Huang, P. Rong, A. Jin, X. Yan, M. G. Zhang, J. Lin, H. Hu, Z. Wang, X. Yue, W. Li, G. Niu, W. Zeng, W. Wang, K. Zhou, X. Chen, *Adv. Mater.* **2014**, *26*, 6401.
- [21] S. H. Yun, S. J. J. Kwok, *Nat. Biomed. Eng.* **2017**, *1*, 0008.
- [22] W. Fan, N. Lu, C. Xu, Y. Liu, J. Lin, S. Wang, Z. Shen, Z. Yang, J. Qu, T. Wang, S. Chen, P. Huang, X. Chen, *ACS Nano* **2017**, *11*, 5864.
- [23] C. Qian, J. Yu, Y. Chen, Q. Hu, X. Xiao, W. Sun, C. Wang, P. Feng, Q. D. Shen, Z. Gu, *Adv. Mater.* **2016**, *28*, 3313.
- [24] Y. Cheng, H. Cheng, C. Jiang, X. Qiu, K. Wang, W. Huan, A. Yuan, J. Wu, Y. Hu, *Nat. Commun.* **2015**, *6*, 8785.
- [25] X. Song, L. Feng, C. Liang, K. Yang, Z. Liu, *Nano Lett.* **2016**, *16*, 6145.
- [26] H. Ren, J. Liu, F. Su, S. Ge, A. Yuan, W. Dai, J. Wu, Y. Hu, *ACS Appl. Mater. Interfaces* **2017**, *9*, 3463.
- [27] G. Ulrich, R. Ziessel, A. Harriman, *Angew. Chem., Int. Ed.* **2008**, *47*, 1184.
- [28] N. Boens, V. Leen, W. Dehaen, *Chem. Soc. Rev.* **2012**, *41*, 1130.
- [29] T. Kowada, H. Maeda, K. Kikuchi, *Chem. Soc. Rev.* **2015**, *44*, 4953.
- [30] G. Fan, Y. X. Lin, L. Yang, F. P. Gao, Y. X. Zhao, Z. Y. Qiao, Q. Zhao, Y. S. Fan, Z. Chen, H. Wang, *Chem. Commun.* **2015**, *51*, 12447.
- [31] S. Bo, C. Song, Y. Li, W. Yu, S. Chen, X. Zhou, Z. Yang, X. Zheng, Z. X. Jiang, *J. Organic Chem.* **2015**, *80*, 6360.
- [32] A. Kamkaew, S. H. Lim, H. B. Lee, L. V. Kiew, L. Y. Chung, K. Burgess, *Chem. Soc. Rev.* **2013**, *42*, 77.
- [33] L. Huang, Z. J. Li, Y. Zhao, J. Y. Yang, Y. C. Yang, A. I. Pendharkar, Y. W. Zhang, S. Kelmar, L. Y. Chen, W. T. Wu, J. Z. Zhao, G. Han, *Adv. Mater.* **2017**, *29*, 1604789.
- [34] Z. Guo, Y. Zou, H. He, J. Rao, S. Ji, X. Cui, H. Ke, Y. Deng, H. Yang, C. Chen, Y. Zhao, H. Chen, *Adv. Mater.* **2016**, *28*, 10155.
- [35] T. Yang, L. Liu, Y. Deng, Z. Guo, G. Zhang, Z. Ge, H. Ke, H. Chen, *Adv. Mater.* **2017**, *29*, 1700487.
- [36] A. Dhawan, V. Sharma, *Anal. Bioanal. Chem.* **2010**, *398*, 589.
- [37] H. He, S. Ji, Y. He, A. Zhu, Y. Zou, Y. Deng, H. Ke, H. Yang, Y. Zhao, Z. Guo, H. Chen, *Adv. Mater.* **2017**, *29*, 1606690.
- [38] J. F. Lovell, J. Chen, M. T. Jarvi, W. G. Cao, A. D. Allen, Y. Liu, T. T. Tidwell, B. C. Wilson, G. Zheng, *J. Phys. Chem. B* **2009**, *113*, 3203.
- [39] H. Lin, Y. Shen, D. Chen, L. Lin, B. C. Wilson, B. Li, S. Xie, *J. Fluoresc.* **2013**, *23*, 41.
- [40] Y. Takaoka, T. Sakamoto, S. Tsukiji, M. Narazaki, T. Matsuda, H. Tochio, M. Shirakawa, I. Hamachi, *Nat. Chem.* **2009**, *1*, 557.
- [41] R. Díaz-López, N. Tsapis, E. Fattal, *Pharm. Res.* **2010**, *27*, 1.
- [42] M. Höckel, P. Vaupel, *JNCI J. Natl. Cancer Inst.* **2001**, *93*, 266.
- [43] H. Maeda, H. Nakamura, J. Fang, *Adv. Drug Delivery Rev.* **2013**, *65*, 71.
- [44] F. Alexis, E. Pridgen, L. K. Molnar, O. C. Farokhzad, *Mol. Pharmaceutics* **2008**, *5*, 505.
- [45] B. K. Park, N. R. Kitteringham, P. M. O'Neill, *Annu. Rev. Pharmacol. Toxicol.* **2001**, *41*, 443.
- [46] P. Agostinis, K. Berg, K. A. Cengel, T. H. Foster, A. W. Girotti, S. O. Gollnick, S. M. Hahn, M. R. Hamblin, A. Juzeniene, D. Kessel, M. Korbelik, J. Moan, P. Mroz, D. Nowis, J. Piette, B. C. Wilson, J. Golab, *Ca-Cancer J. Clin.* **2011**, *61*, 250.
- [47] L. Cheng, C. Wang, L. Feng, K. Yang, Z. Liu, *Chem. Rev.* **2014**, *114*, 10869.
- [48] W. Fan, P. Huang, X. Chen, *Chem. Soc. Rev.* **2016**, *45*, 6488.